Materials Research. 2020; 23(2): e20190678
DOI: https://doi.org/10.1590/1980-5373-MR-2019-0678

Influence of Different Concentrations of Silicon, Copper and Tin in the Microstructure and in the Mechanical Properties of Compacted Graphite Iron

B. C. M. Ribeiro[a,b], F. M. Rocha[b], B. M. Andrade[a], W. Lopes[a], E. C. S. Corrêa[a*]

[a] *Centro Federal de Educação Tecnológica de Minas Gerais (CEFETMG), Departamento de Engenharia de Materiais, Avenida Amazonas, 5253, Nova Suíça, 30.421-169, Belo Horizonte, MG, Brasil*
[b] *TEKSID do Brasil, Rua Senador Geovane Agnelli, 230, Distrito Industrial Paulo Camilo Sul, 32.671-072, Betim, MG, Brasil*

Received: December 16, 2019; Accepted: April 2, 2020

In this paper the production and characterization of compacted graphite iron alloys in ten chemical compositions is presented. The specimens were obtained through a foundry process performed by a gating system model developed in order to allow the incorporation of silicon, copper and tin. Hardness and tensile tests were performed, as well as microstructural evaluation. Additionally, the results related to the experimental investigation were compared to those obtained from a finite element method analysis. The results showed a correlation between the addition of silicon and the increase of ferrite and graphite count per mm^2. Regarding copper and tin additions, the percentage increase of pearlite was associated with the reduction of graphite average size. Changes in chemical composition led to different values of ultimate tensile strength, yield strength and hardness, whose magnitude was mainly related to the amount of ferrite. Computer simulation was considered efficient in predicting these results.

Keywords: *Compacted graphite iron, microstructure, mechanical properties, computational simulation.*

1. Introduction

The microstructure of compacted graphite iron alloy (CGI) is composed by graphite particles scattered in a metal matrix, usually consisting of pearlite or pearlite and ferrite[1,2]. Graphite resembles a worm-like structure with fairly thick particles, elongated, showing no orientation and with round endings, forming a interconnected three-dimensional network over the material, whose morphology is intermediate between that observed in gray cast iron and in ductile cast iron[3-5]. This intermediate morphology of the graphite, combined with the metal matrix, provides a combination of mechanical and physical properties which are also intermediate between gray and ductile cast irons. Due to this morphology, CGI alloys have good mechanical strength, toughness, enhanced thermal conductivity and the additional capacity of vibration damping, which testifies in favor of their use as an alternative to gray cast iron alloys in engine applications that require higher limits of pressure, allowing the reduction of engine's weight and size without undermining their efficiency[6-8]. Altogether, these properties turn compacted graphite iron alloys into a big prospect for the automotive industry, especially considering the manufacture of cylinder block and cylinder head for diesel engines[8].

The chemical composition of the CGI alloy is crucial in determining the proportions of pearlite and ferrite in the matrix and in the graphite distribution, size and morphology, affecting the mechanical properties of the material. As a result, specific chemical elements might be introduced into cast irons aiming to adjust and/or alter its characteristics. Silicon is a graphitizing element, generally favouring the solidification according to the stable form in the phases diagram[9]. Mg and Ce influence the morphology of the graphite and their presence is connected to the increase in ductility[10]. Sulfur also influences graphite morphology, favouring lamellar graphite formation[11]. Initially, copper and tin favour the formation of pearlite and are important in increasing the mechanical strength of the material[12-15]. Investigations regarding chromium focus mainly on its carbide promoting properties, showing also its pearlitizing action[16].

In this context, the present investigation involves the analysis of the influence of different amounts of silicon, copper and tin in graphite's characteristics, in the matrix and in the mechanical properties of CGI. Aiming this purpose, hardness and tensile test were conducted. Furthermore, computer simulations were carried out and the results were compared with those obtained through the experiments, in order to verify the reliability of the simulation in predicting other conditions of chemical composition.

2. Materials and Methods

2.1 Manufacture of test specimens

Aiming the manufacture of specimens through foundry, a gating system was created, Figure 1, in which "Y" block size was developed according to ASTM A536-84[17]. The gating system allowed the simultaneous and symmetric confection of two test specimens, considered identical, with the goal of

*e-mail: *elainecarballo@cefetmg.br*

obtaining the same microstructure characteristics, mechanical properties and chemical composition.

In Figure 1 the specimens embodied are showed: i) a pouring cup, aiming the pouring of liquid metal to feed the system; ii) sprue, runners and gates, in order to fill the test specimens; iii) a slag retainer, in order to retain residual slag; iv) a filter, projected to keep potential sand or remnant slags from hitting the specimen; and v) a reaction chamber, enabling the introduction of silicon, copper and tin into the specimen. It is important to emphasize the use of the reaction chamber in industry in in-mold processes as an alternative to the manufacture of ductile cast iron[18]. In this work, the reaction chamber was used to allow the introduction of different percentages of silicon, tin and copper.

After the construction of the gating system, a model for the confection of the sand mold was developed. Ten molds were built based on this model, using the same sand mixture, resin and catalyser. Amounts of different alloys were placed inside of the reaction chamber of each mold allowing the incorporation of different percentages of Si through the introduction of predetermined amounts of FeSi. Similarly, aiming the incorporation of different percentages of Sn and Cu, different amounts of those alloys were introduced into the reaction chambers. The amount of alloy introduced into the reaction chamber (Q_l) was calculated based on the following parameters: i) the percentage of the chemical element aimed to be embodied ($\%_{incorp.}$); ii) the weight of metal needed to fill the test specimens and the gating system (Wm), equals 28 kg, and iii) the output of the alloy introduced into the reaction chamber (γ). This output relates to the percentage of the chemical element present in the alloy. The output is 100% for Sn and Cu alloys, but 75% for the embodiment of Si from FeSi. Equation 1 shows the relationship from which the amount of alloy placed into the reaction chamber was calculated according to the percentage of incorporation intended, whose results are presented in Table 1.

$$Q_l = \frac{Wm \times (\%_{incorp.})}{Y} \quad (1)$$

The experiments were performed with a compacted graphite iron alloy obtained from conventional foundry and the chemical composition was adjusted through SinterCast's equipment patent number 5337799 (1994). The final chemical composition in standard condition is found in Table 2.

From the standard chemical composition, ten different chemical compositions were obtained, as shown in Table 3. The pouring temperature was 1420º C and the demolding time was 30 minutes for all ten testing conditions.

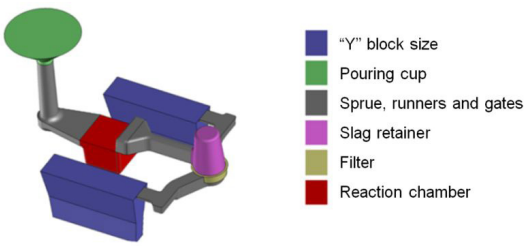

Figure 1 – Gating system associated to "Y" block size.

2.2 Materials characterization

Optical microscopy, scanning electron microscopy, Brinell hardness and tensile test were employed in this investigation.

Considering microstructural characterization, the samples were submitted to conventional metallographic preparation methods and the chemical attack was performed with Nital 3%. The analysis and acquisition of images were performed in two steps using a Fortel optical microscope (OM). Prior to the chemical attack, all samples were photographed in order to observe the morphology and the dimension of the compacted graphite. After chemical attack, new images were obtained in order to evaluate the effects of different chemical compositions in ferrite and pearlite proportions.

The analysis of graphite morphology was performed with an image analysis software, by measuring the area of the graphite veins in thirty images from samples without the chemical attack. In addition, the amount of graphite per mm^2 and the compacted and ductile graphite proportions were evaluated. The images after the chemical attack were analyzed in the same software. In addition to optical microscopy, scanning electron microscopy (SEM) using secondary electrons was employed in this work. At this point, the influence of the chemical composition in pearlite interlamellar spacing

Table 1 – Amount of alloy added to the reaction chamber for the percentage increase of chemical composition.

Molde	Designation	Ql	The expected increase of the chemical element
Mold 1	Standard Condition (Ao)	0.0 g	-
Mold 2	Silicon 1 (Si_1)	56.0 g	0.15%
Mold 3	Silicon 2 (Si_2)	112.0 g	0.30%
Mold 4	Silicon 3 (Si_3)	168.0 g	0.45%
Mold 5	Copper 1 (Cu_1)	42.0 g	0.15%
Mold 6	Copper 2 (Cu_2)	84.0 g	0.30%
Mold 7	Copper 3 (Cu_3)	126.0 g	0.45%
Mold 8	Tin 1 (Sn_1)	4.2 g	0.015%
Mold 9	Tin 2 (Sn_2)	8.4 g	0.030%
Mold 10	Tin 3 (Sn_3)	12.6 g	0.045%

Table 2 – Average of the chemical analysis in standard condition.

Condition	%C	%Si	%Cu	%Sn	%Mn	%S	%P
A_0	3.71	2.10	0.61	0.060	0.41	0.011	0.051

Table 3 – Test specimens obtained from different chemical compositions.

Condition	%C	%Si	%Cu	%Sn	%Mn	%S	%P
A_0	3.71	2.10	0.61	0.060	0.41	0.011	0.051
Si_1	3.71	**2.25**	0.60	0.061	0.41	0.010	0.051
Si_2	3.72	**2.39**	0.61	0.060	0.42	0.011	0.050
Si_3	3.70	**2.54**	0.61	0.059	0.41	0.012	0.051
Cu_1	3.71	2.10	**0.75**	0.061	0.42	0.013	0.052
Cu_2	3.71	2.11	**0.90**	0.060	0.41	0.011	0.050
Cu_3	3.69	2.09	**1.04**	0.062	0.41	0.010	0.050
Sn_1	3.71	2.10	0.60	**0.075**	0.40	0.011	0.051
Sn_2	3.72	2.10	0.61	**0.091**	0.43	0.011	0.051
Sn_3	3.71	2.09	0.61	**0.105**	0.42	0.012	0.053

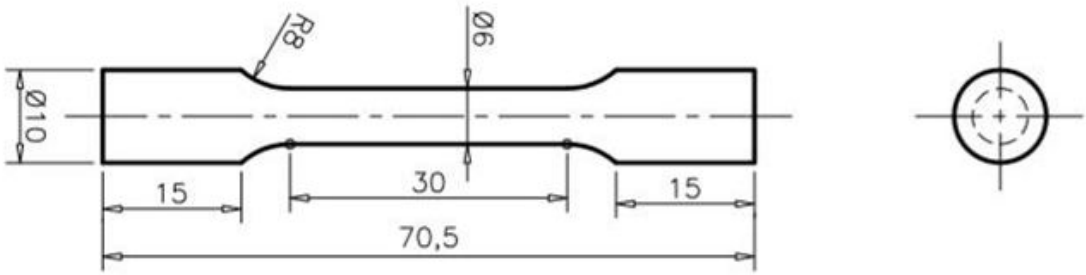

Figure 2 – Dimensions of test specimens used in tensile testing.

was analyzed. The analysis was performed in a Shimadzu SSX-550 Superscan scanning electron microscope.

Brinell hardness tests were performed in a Metro Com Macchine per Prove Material durometer. The load was 750 kgf, the penetration time was 15 s and the indenter was a steel sphere with 5 mm diameter. Each sample was measured ten times.

Tensile tests were performed in an Instron 5982 universal testing machine, with Blue Hill 3 control system. In order to acquire deformation values, an automatic Instron 2630-100 extensometer was employed in the experiments. The cross-head speed was 1.7 mm/min, leading to an initial deformation rate of $10^{-3}s^{-1}$. Yield strength, ultimate tensile strength and uniform elongation values were calculated according to ASTM A370[19]. Four test specimens were machined for each condition, according to ASTM E8/E8M 16a[20], employing sub size dimensions, proportional to the standard. Figure 2 shows the test specimens used during tensile tests.

Figure 3 shows the schematic drawing of "Y" block size emphasizing the places from where the four test specimens were machined for tensile and impact tests. Samples for the chemical composition analysis, metallography and Brinell hardness tests were taken from the central areas of test specimens, signaled as 5.

2.3 Computer simulation

The computer simulation was conducted in MAGMASOFT® software. This software estimates mechanical properties and final characteristics from alloys melted according to the chemical and metallurgical parameters related to the manufacturing of the piece. A mesh with 125000 elements was used in the simulations. Figure 4 presents the image of the mesh adopted in the simulations and an example of the standard condition simulation to check the material ultimate tensile strength.

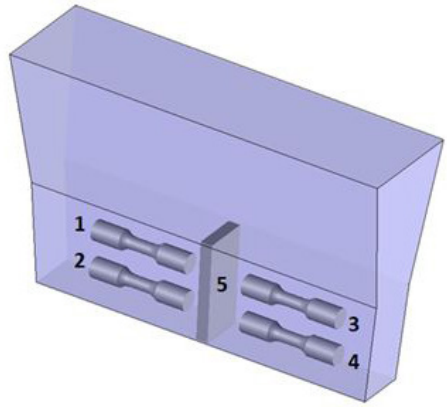

Figure 3 – Position of the specimens and sample in test block size Y.

3. Results and Discussion

3.1 Microstructural characterization

3.1.1 Material characterization in standard chemical composition

OM and SEM images obtained from samples in the initial state are presented in Figure 5. The matrix shows primarily pearlite and graphite in compacted morphology. The sample hardness was 238 ± 6.3 HB. Graphite's area

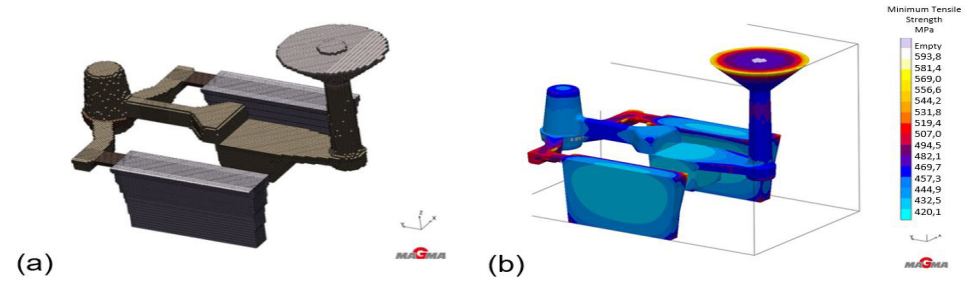

Figure 4 – (a) Image of the netting adopted in computer simulations and (b) example of simulation.

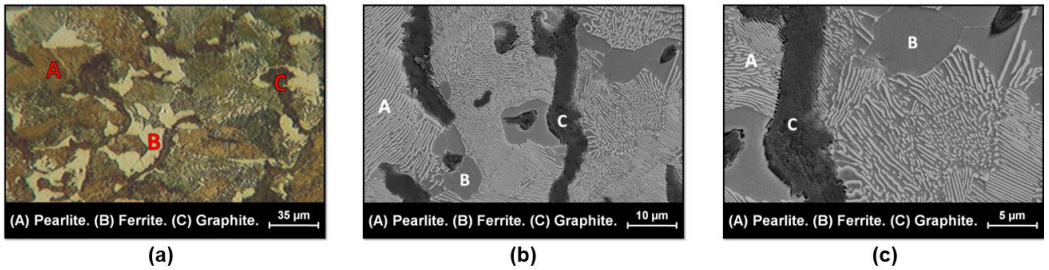

Figure 5 – Metallographic analysis of the sample in the initial state: (a) OM, (b) and (c) SEM

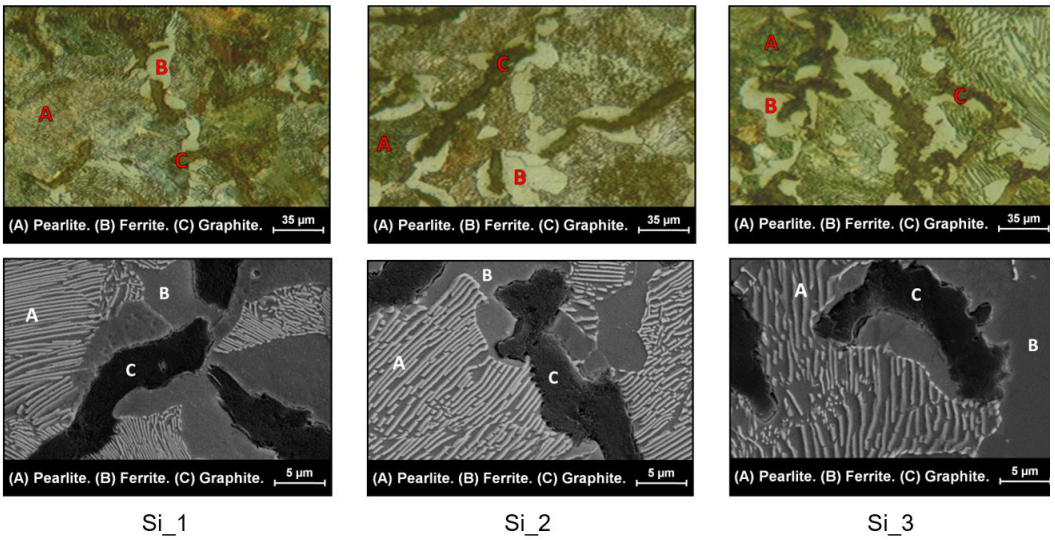

Figure 6 – OM and SEM micrographs of the CGI at different silicon levels.

had on average 3654.8 µm^2. The material presented 10.9% of ductile graphite and 89.1% of compacted graphite, as recommended by ASTM A842-85[21], which admits a minimum percentage of 80% of compacted graphite to consider the alloy as a CGI, not presenting lamellar graphite.

3.1.2 Microstructural analysis of silicon added test specimens

Figure 6 shows the microstructure of the samples with gradual addition of silicon. There is an increase in ferritic regions replacing pearlite as the percentage of silicon raises in the sample. Furthermore, SEM images show an increase of pearlite interlamellar spacing. The compacted graphite and ductile graphite proportions showed no significant changes as silicon levels increase when compared to the samples in standard condition, keeping their values close to 10% for ductile graphite and 90% for compacted graphite.

The results of quantitative microstructural analysis are shown in Figure7. It is possible to observe the increase of ferritic regions replacing pearlite and the greater amount of graphite per mm^2 in samples with higher percentage of silicon. It is also observed a slight increase on the average area of the graphite as the percentage of silicon raises.

The addition of silicon in cast irons has pronounced effects in their microstructure. The graphitizing effect is one of them, associated to the amount of free carbon in graphitic structures. Silicon addition favours solidification according to the stable form of the phases diagram, in which cementite stability is reduced during the eutectoid reaction, leading carbon atoms to deposit and grow preferably by the cores

previously established during the inoculation of the alloy[9]. Therefore, regions alongside graphite veins are deprived in carbon in solution, increasing the occurrence of ferrite in those areas[14,16]. Additionally, the introduction of silicon alloys moments prior to the pouring of specimens or pieces characterizes the process of inoculation. In the present work, the addition of FeSi took place in the reaction chamber, characterizing an inoculation as well. The inoculation correlates directly to the amount of nuclei created for graphite growth. The bigger the amount of inoculant, the more nuclei is formed, enabling uniform distribution of graphite particles during their growth[16]. This phenomenon was progressively observed, the graphite amount per mm^2 and the percentage of ferrite in the microstructure increased to the extent of FeSi increase in the reaction chamber. In addition to the graphitizing effect, silicon increases the temperature range during which austenite and ferrite coexist, raising the range of temperature that allows a stable transformation. Thus, there is more time available for the diffusion of carbon during solidification, favoring a longer carbon diffusion, that leads to the increase of pearlite interlamellar spacing[22].

3.1.3 Microstructural analysis of copper added test specimens

The microstructure of the samples with progressive copper addition is shown in Figure 8. The reduction of ferritic fraction is verified as the percentage of copper increases. Furthermore, SEM images show a slight decrease in pearlite interlamellar spacing due to the increase in copper levels. Similarly to the results related to silicon, the compacted and ductile graphite proportions showed no significant variation with copper addition, around 90% for compacted graphite and 10% for ductile graphite.

Through the analysis of Figure 9, it is possible to notice a reduction in the average area of the graphite in the microstructure, as the percentage of copper increases. This

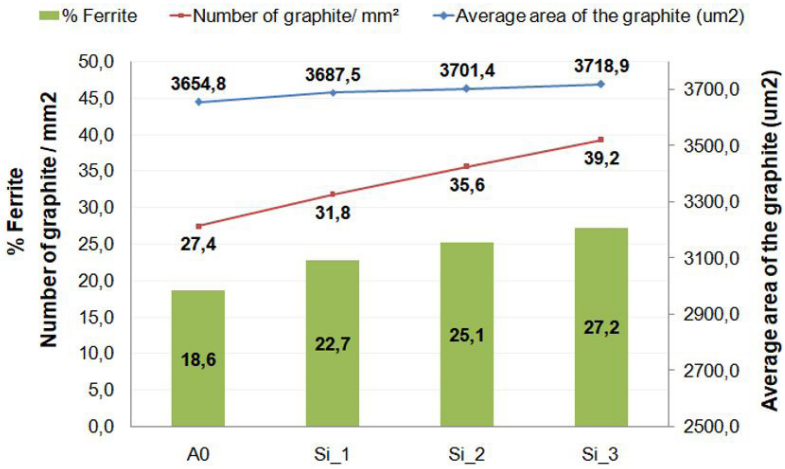

Figure 7 – Percentual of ferrite and graphite's area and quantity.

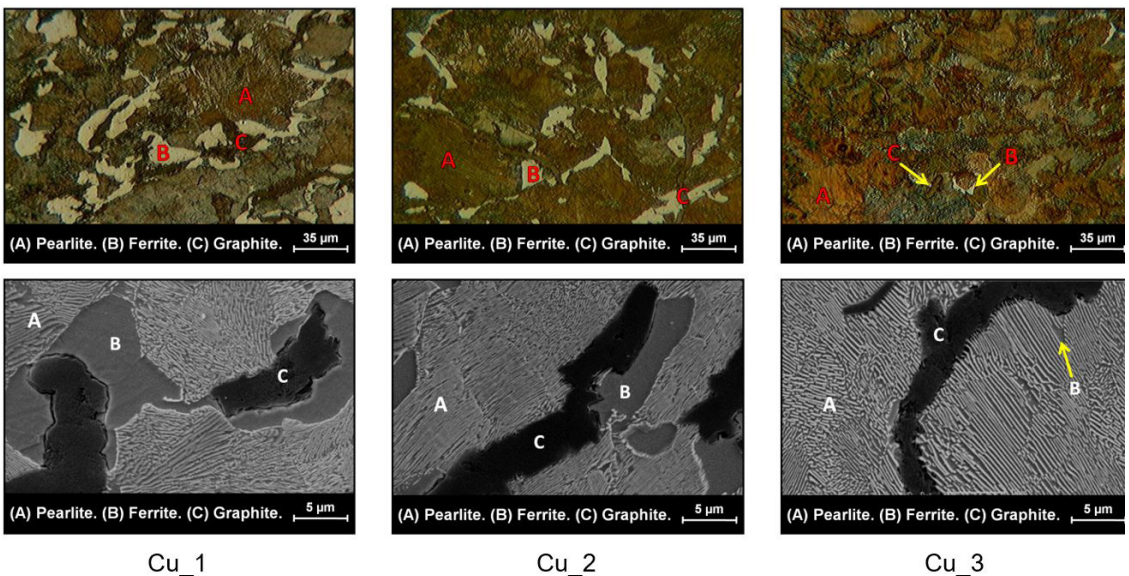

Figure 8 – OM and SEM micrographs of the CGI at different copper levels.

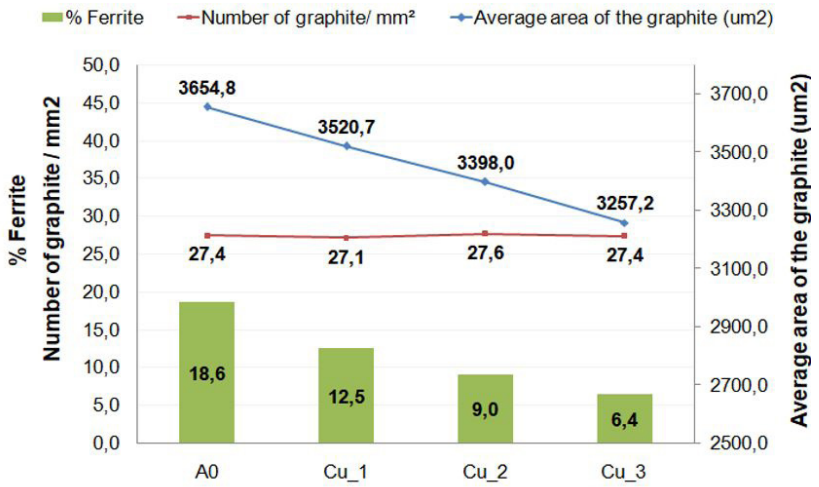

Figure 9 - Percentual of ferrite and graphite's area and quantity.

reduction of the average area was followed by the percentage reduction of ferrite.

The pearlitizing effect of copper is associated with its barrier forming properties, allowing the formation of a barrier in graphite surface which inhibits carbons diffusion from the matrix to graphite. This inhibition allows a greater carbon concentration in the matrix, favouring the formation of pearlite over ferrite. Present results show that the percentage increase of copper led to a greater ratio of pearlite in the material and a reduction of graphite average area, indicating a decrease in carbon diffusion to graphite particles[9,16]. In addition to the pearlitizing effect, copper reduces the range temperature in which austenite and ferrite coexist, reducing the range of temperature that allows a stable transformation. Therefore, carbon has a reduced time gap to diffuse during solidification, impairing carbon diffusion to longer distances and diminishing pearlite interlamellar spacing.

3.1.4 Microstructural analysis of tin added test specimens

The microstructure of the samples with progressive addition of tin is shown in Figure 10. Resembling the results found in copper added samples, there is a reduction on ferritic regions as the percentage of tin increases in the sample, as well as a reduction of pearlite interlamellar spacing. Similarly to previous results, the compacted graphite and ductile graphite ratio showed no significant variations with the addition of tin when compared to the standard alloy.

Figure 11 shows the reduction in graphite average area in the microstructure according to the percentage increase of tin, comparably to copper added samples. This average reduction in graphite area was followed by a percentage reduction of ferrite. Opposite to the results presented by silicon alloys, there was no pronounced variation in the graphite amounts per mm^2.

Tin pearlitizing characteristics are very similar to those found in copper, showing also barrier forming properties that impair carbon diffusion in the material and that might ultimately lead to graphite deterioration when in high amounts. Tin application might also reduce the ductility and the material resistance to fatigue. Comparing copper and tin pearlitizing properties, literature indicates that tin pearlitizingability is ten times stronger than copper[14]. Present results confirm tin's higher tendency of pearlitization by the greater reduction of ferrite percentages, leading to lower proportions than those achieved in copper alloys, even when tin levels in the chemical composition are ten times lower. This phenomenon is related to a stronger reduction of the driving force required for cementite nucleation, favouring the formation of pearlite with smaller interlamellar spacing, due to the reduction of cooling rates for pearlite nucleation[13,16]. The mechanism behind this effect involves tin segregation in graphite and austenite interface. According to Jacques and Jon[14], the transient formation of Fe_3SnC is more likely to happen in the graphite and austenite interface during the post-solidification cooling, inhibiting carbons diffusion. Therefore, the percentage increase of tin leads to the increase in pearlite ratio and the inhibition in carbon diffusion to graphite, limiting graphite growth. The results in this investigation demonstrate that alloys with a higher percentage of tin show smaller graphite average sizes and lower ferrite ratios. Similarly to copper, tin addition also reduces temperature ranges in which austenite and ferrite coexisted. Thus, there is a reduced time gap for carbon diffusion during solidification, favouring a decrease in pearlite interlamellar spacing.

3.2 Mechanicalcharacterization

3.2.1 Hardness analysis

The results for hardness testing, organized in ascending order and associated to the ferrite ratio, are shown in Figure 12. There is an increase in hardness followed by a reduction in ferrite percentage. The results show a correspondence between the increase in Cu and Sn levels and hardness, with a consequent reduction in ferrite percentages. On the other hand, as silicon levels increased, there was a reduction in hardness, followed by an increase in ferrite. In addition to the ferrite influence, consequence of Si, Cu and Sn inclusion, changes in pearlite interlamellar spacing also affected hardness

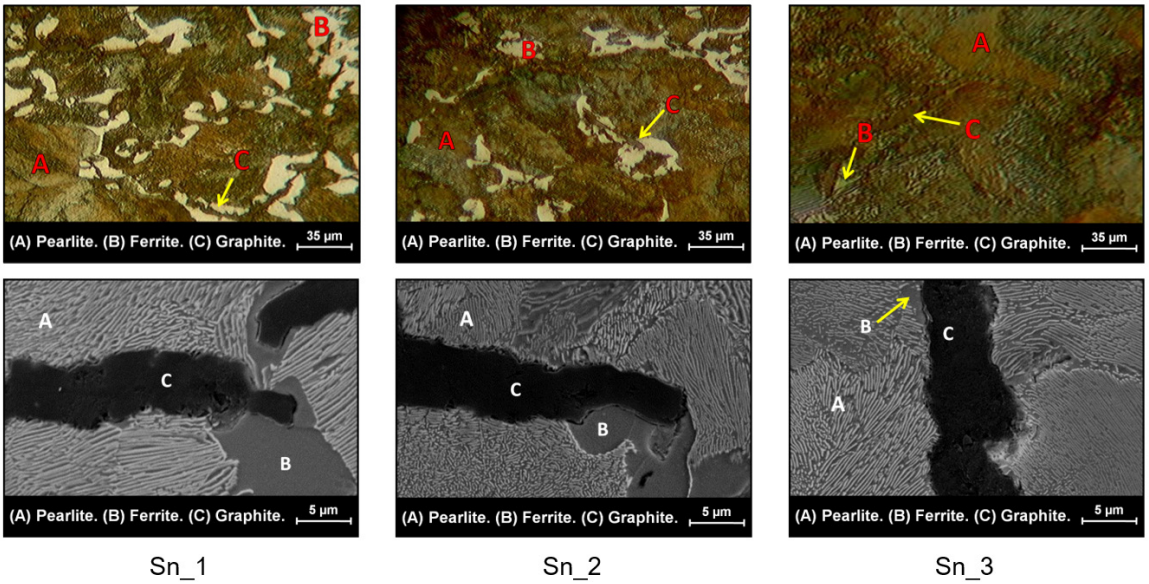

Figure 10 – OM and SEM micrographs of the CGI at different tin levels.

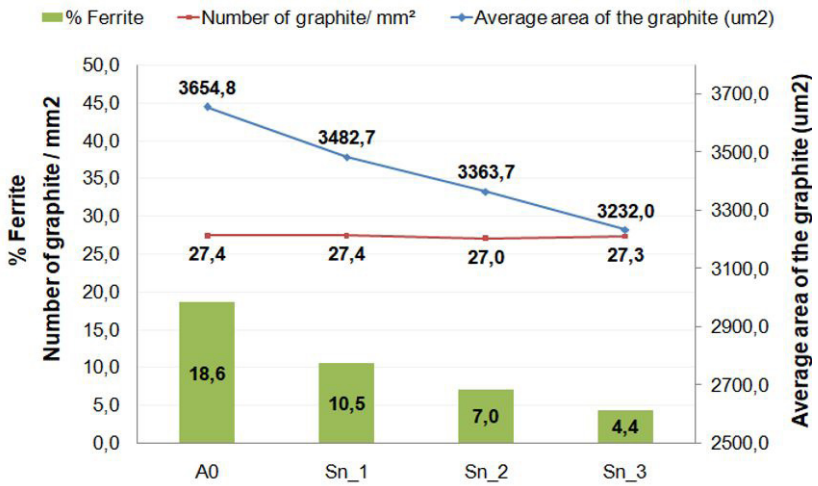

Figure 11 – Percentual of ferrite and graphite's area and quantity.

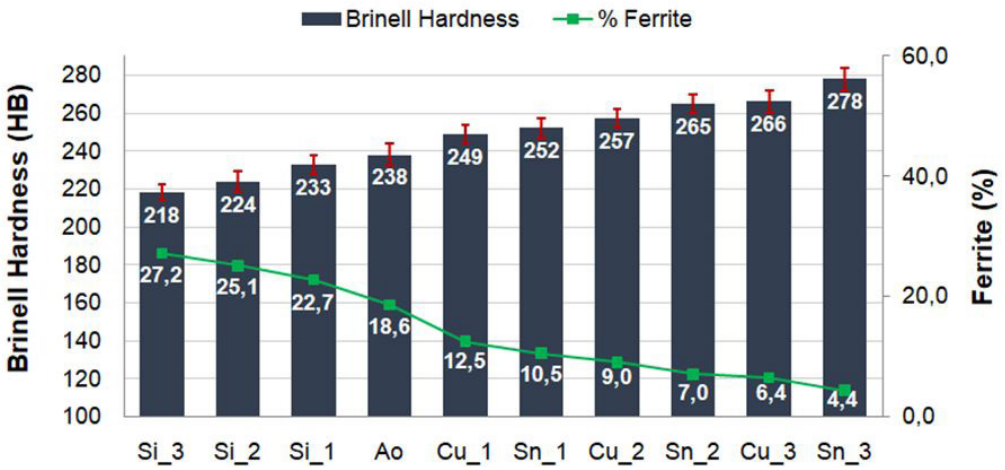

Figure 12 – Brinell Hardness results.

values, considering that, generally, shorter spaces produce a greater hardness[23].

3.2.2 Tensile testing

Figure 13 presents ultimate tensile strength, yield strength and uniform elongation values, obtained from tensile testing. Samples were organized in ascending order considering the ultimate tensile strength. Test specimens with the lowest ultimate tensile strength and the lowest yield strength are the ones with higher ferrite percentages. The uniform elongation presented also a slight reduction in samples with lower ferrite percentages. Furthermore, similarly to hardness analysis, these results might also be affected by pearlite interlamellar spacing. Comparing ultimate tensile strength, yield strength and elongation results with those presented in ISO 16112/ 2017[24], it is possible to notice that the values obtained in this investigation fit into the compacted graphite iron category, according to the classes JV 450 and JV 500, which show ultimate tensile strength values between 450 and 575 MPa; yield strength between 315 and 400 MPa and elongation ranging from 0,5 to 2,0%.

3.3 Computer simulation

Figures 14 to 16 show the results for the mechanical properties obtained through numerical simulation, in comparison to those from the experiments. Tendencies observed in test

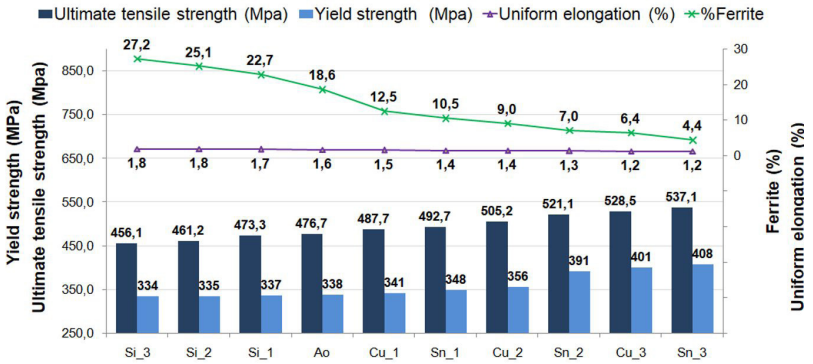

Figure 13 – Tensile testing results.

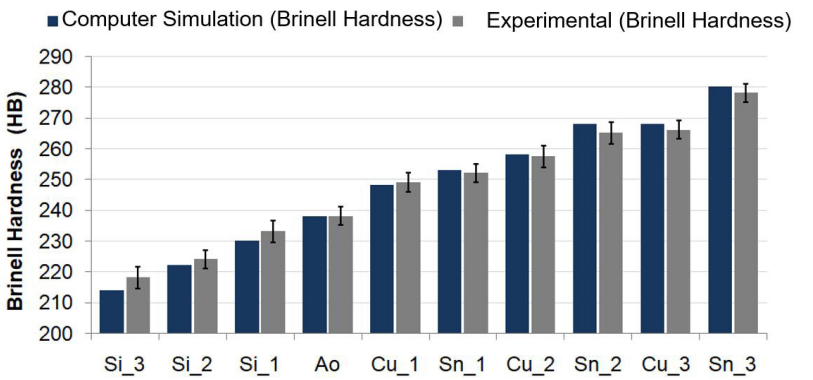

Figure 14 – Brinell Hardness results.

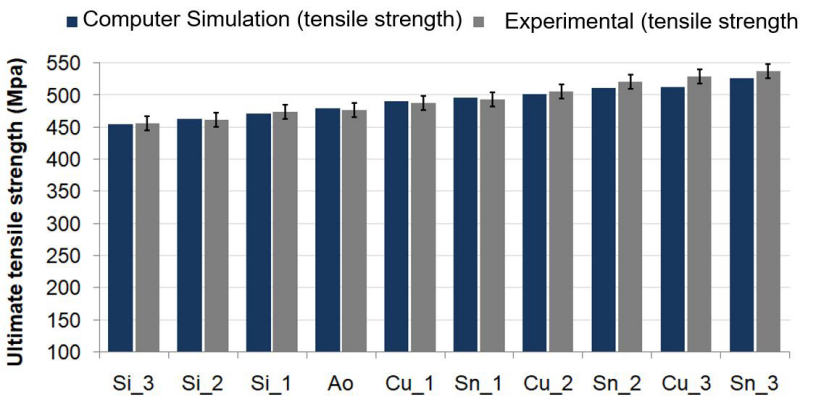

Figure 15 – Ultimate tensile strength results.

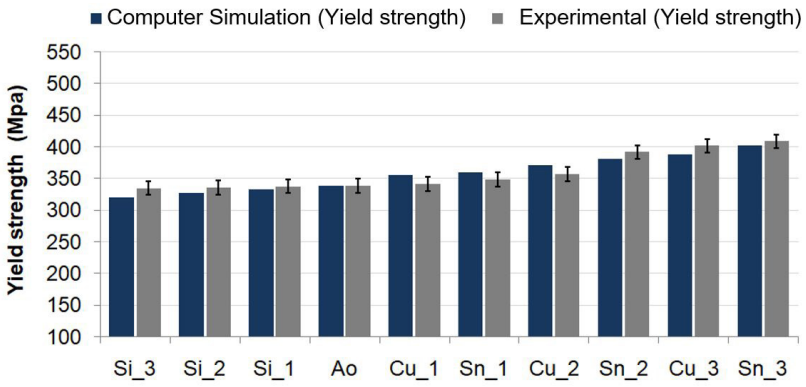

Figure 16 – Yield strength results.

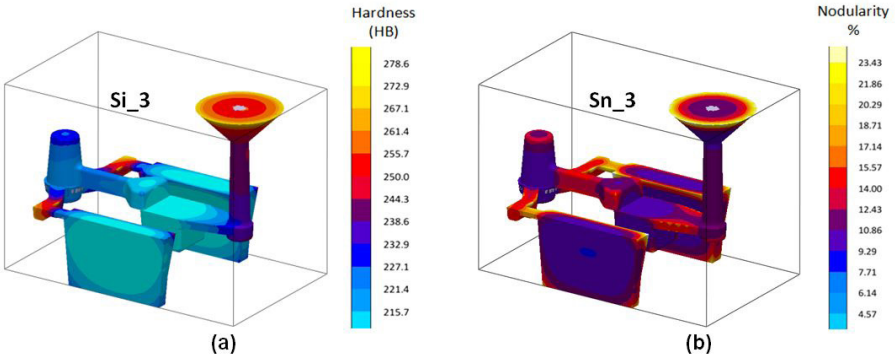

Figure 17 – (a) Test run to verify hardness; (b) Test run to verify the ductile graphite percentage.

results were similar to the numeric data, specifically when taking standard deviation into consideration, even though, there were differences between both results. Therefore, the simulation was considered an efficient tool in determining the performance of CGI alloys. In this context, computer simulation has potential to be used in predicting results from chemical compositions other than those evaluated in the present investigation, among other possible analysis. Figure 17 shows also results for the ductile graphite ratio from the condition Sn_3 and hardness results for the condition Si_3, from which it is possible to verify the homogeneity among the microstructure of the alloys and the properties evaluated.

4. Conclusions

- The addition of silicon, copper and tin did not lead to changes in the ratio between compacted and ductile graphite.
- The silicon added alloys developed microstructures with an increase of ferritic regions combined with an increase in the graphite amount per mm^2. The increase in silicon levels led to a reduction in hardness, yield strength, and ultimate tensile strength values.
- The percentage increase in copper and tin led to an increase in the pearlite proportion. Furthermore, there was a decrease in graphite average area accompanying the increase in Cu and Sn levels. The increase in pearlitizing elements led to an increase in the material's hardness, yield strength and ultimate tensile strength.
- The comparison between copper and tin pearlitizing power, demonstrated the superior pearlitizing power of Sn in relation to copper, reaffirming literature data.
- Computer simulation predicted similar values to those obtained from experimental testing, regarding yield strength, ultimate tensile strength and hardness.

5. Acknowledgments

The authors are grateful toTEKSID do Brasil, to CEFET-MG (Centro Federal de Educação Tecnológica de Minas Gerais), to CNPq (Conselho Nacional de Desenvolvimento Científico e Tecnológico), to CAPES (Coordenação de Aperfeiçoamento de Pessoal de Nível Superior) and to FINEP (Financiadora de Inovação e Pesquisa).

6. References

1. Quiu Y, Pang JC, Zouc CL, Zhang MX, Li SX, Zhang ZF. Fatigue strength model based on microstructures and damage mechanism of compacted graphite iron. Mater Sci Eng A. 2018;724:324-9.
2. Lacaze J. Pearlite growth in cast irons: a review of literature data. Int J Cast Met Res. 1999;11:431-6.
3. Zhang YY, Pang JC, Shen RL, Qiu Y, Li SX, Zhang ZF. Investigation on tensile deformation behavior of compacted graphite iron based on cohesive damage model. Mater Sci Eng A. 2018;713:260-368.

4. Mrzygłód B, Gumienny G, Wilk-Kołodziejczyk D, Regulski K. Application of Selected Artificial Intelligence Methods in a System Predicting the Microstructure of Compacted Graphite Iron. J Mater Eng Perform. 2019;28:3894-904.
5. Chuang C, Singh D, Kenesei P, Almer J, Hryn J, Huff R. Application of X-ray computed tomography for the characterization of graphite morphology in compact-graphite iron. Mater Charact. 2017;141:442-9.
6. Mohammed WM, Ng E, Elbestawi MA. Modeling the effect of the microstructure of compacted graphite iron on chip formation. Int J Mach Tools Manuf. 2011;51:753-65.
7. Gumienny G, Kacprzyk B. Copper in ausferritic compacted graphite iron. Archives of Foundry Engineering. 2018;18:162-6.
8. Steve D. Compacted graphite iron - a material solution for modern engine design. SAE International. 2011;1083:1-6.
9. Liu Y, Xing J, Li Y, Wang Y, Wang L, Zheng B. Effect of carbon equivalent on thermal and mechanical properties of compacted graphite cast iron. J Mater Res. 2016;31:2516-23.
10. Chakraborty S, Gadkari S, Steinmetz P, Monroe CA, Genau AL. Evolution of microstructure in directionally solidified cast iron treated with cerium and magnesium. The minerals. Metals & Materials Society and ASM International. 2019;50:2922-32.
11. Bazdar M, Abbasi HR, Yaghtin AH, Rassizadehghani J. Effect of sulfur on graphite aspect ratio and tensile properties in compacted graphite irons. J Mater Process Technol. 2019;209:1701-5.
12. Lacaze J, Sertucha J. Effect of tin on the phase transformations of cast irons. J Phase Equilibria Diffus. 2017;38:743-9.
13. Sertucha J, Larranaga P, Lacaze J, Insausti M. Experimental investigation on the effect of copper upon eutectoid transformation of as-cast and austenitized spheroidal graphite cast iron. Int J Met Cast. 2010;10:51-8.
14. Lacaze J, Sertucha J. Effect of Cu, Mn and Sn on pearlite growth kinetics in as-cast ductile irons. Int J Cast Met Res. 2016;29(1-2):74-8.
15. Lacaze J, Boudot A, Gerval V, Oquab D, Santos H. The role of manganese and copper in the eutectoid transformation of spheroidal graphite cast iron. Metall Mater Trans, A Phys Metall Mater Sci. 1997;28:2015-25.
16. König M, Wessén M. Influence of alloying elements on microstructure and mechanical properties of CGI. Int J Cast Met Res. 2010;23:97-110.
17. ASTM: American Society for Testing and Materials. ASTM A536-84 – Standard Specification for Ductile Iron Castings. West Conshohocken: ASTM International; 2019.
18. Borsato T, Berto F, Ferro P, Carollo C. Effect of in-mould inoculant composition on microstructure and fatigue behaviour of heavy section ductile iron castings. Procedia Structural Integrity. 2016;2:3150-7.
19. ASTM: American Society for Testing and Materials. ASTM A370 – Standard Test Methods and Definitions for Mechanical Testing of Steel Products. West Conshohocken: ASTM International; 2014.
20. ASTM: American Society for Testing and Materials. ASTM E8/E8M – Standard Test Methods for Tension Testing of Metallic Materials. West Conshohocken: ASTM International; 2016.
21. ASTM: American Society for Testing and Materials. ASTM A842-85 – Standard Specification for Compacted Graphite Iron Castings. West Conshohocken: ASTM International; 2009.
22. Krauss G. Steels heat treatment and processing principles. ASM International; 1989. p. 17-21.
23. Reed-Hill RE. Phisycal metalurgy principles 3rd ed. New York: Van Nostrand Reinhold; 1994.
24. ISO: International Organization for Standardization. ISO 16112: 2006 – Standard Specification for Compacted (vermicular) graphite cast irons – Classification. Geneva: ISO International Organization for Standardization; 2006.